*Clay Minerals*, (2015) **50**, 619–638

# Influence of phyllosilicates and fluid–rock interaction on the deformation style and mechanical behaviour of quartz-rich rocks in the Carboneras and Palomares fault areas (SE Spain)

J. JIMÉNEZ-MILLÁN*, I. ABAD, P. HERNÁNDEZ-PUENTES AND R. JIMÉNEZ-ESPINOSA

*Department of Geology, University of Jaén. 23071 Jaén, Spain*

(*Received 21 January 2015; revised 4 October 2015; Associate Editor: Juan Cornejo*)

ABSTRACT: Deformed quartzitic rocks from the Carboneras and Palomares fault areas (SE Spain) are enriched in phyllosilicates compared to their respective protoliths. Deformation is mainly localized in highly foliated chlorite-rich bands. Quartz-rich bands show brittle deformation developing dolomite-rich cross-cutting veins re-cementing microcataclasite areas. Undamaged lenses within the cataclastic rocks contain patches of phyllosilicates with randomly oriented chlorite and mica. Mg, Fe, water, As and Zn enrichment of the damaged rocks suggests a process of hydrothermal chloritization associated with the Cabo de Gata volcanism. Petrographic characteristics indicate that hydrothermal alteration that produced chlorite and mica-enrichment occurred before faulting. Phyllosilicates provided lubricating properties to the quartzitic rocks, favouring the predominance of creep over seismic stick-slip and reducing the possibility of large seismogenic events. Dolomite cementation as a consequence of fluid–rock interaction processes would have a limited effect, due to the presence of weak phyllosilicate surfaces.

A number of competing effects that include fault composition, lithification state, thickness and internal structure affect the strength of natural faults (Tesei *et al.,* 2012). Most quartzo-feldspathic materials have a strong and fragile behaviour due to their high friction coefficients ($\mu \approx 0.6$–$0.7$, Byerlee, 1978; Dieterich & Kilgore, 1994). Because to these features, the style of deformation of phyllosilicate-poor fault rocks is generally characterized by the presence of blocks where strain is highly localized, with abundant polished and striated fault surfaces. Deformation mechanisms during the development of upper crustal fault zones in quartzitic rocks commonly involve fracture, low-temperature crystal plasticity and diffusion mass-transfer processes (Lloyd *et al.*, 1992). However, inherited microstructures present in the parent materials (*e.g.* grain size, sorting, packing and contact area, cement and matrix phases such as clays) may have a crucial role in influencing deformation processes.

The presence of phyllosilicates in fault zones as either neoformed or inherited clays is commonly related to mechanically weak fault behaviour (*e.g.* Wang, 1984; Lachenbruch & Sass, 1988; Zoback, 2000; Solum & Van der Pluijm, 2004, Ikari *et al.*, 2011; Tesei *et al.*, 2012). Low friction coefficients of phyllosilicates (in general $\mu < 0.4$ for a great number of phyllosilicates) have been invoked to justify this weakness and creeping behaviour of faults under a variety of crustal conditions. A critical factor for the understanding of the mechanical role of clays in fault rocks is to determine the timing of formation of mineral

*Email: jmillan@ujaen.es
DOI: 10.1180/claymin.2015.050.5.06

© 2016 The Mineralogical Society
https://doi.org/10.1180/claymin.2015.050.5.06 Published online by Cambridge University Press

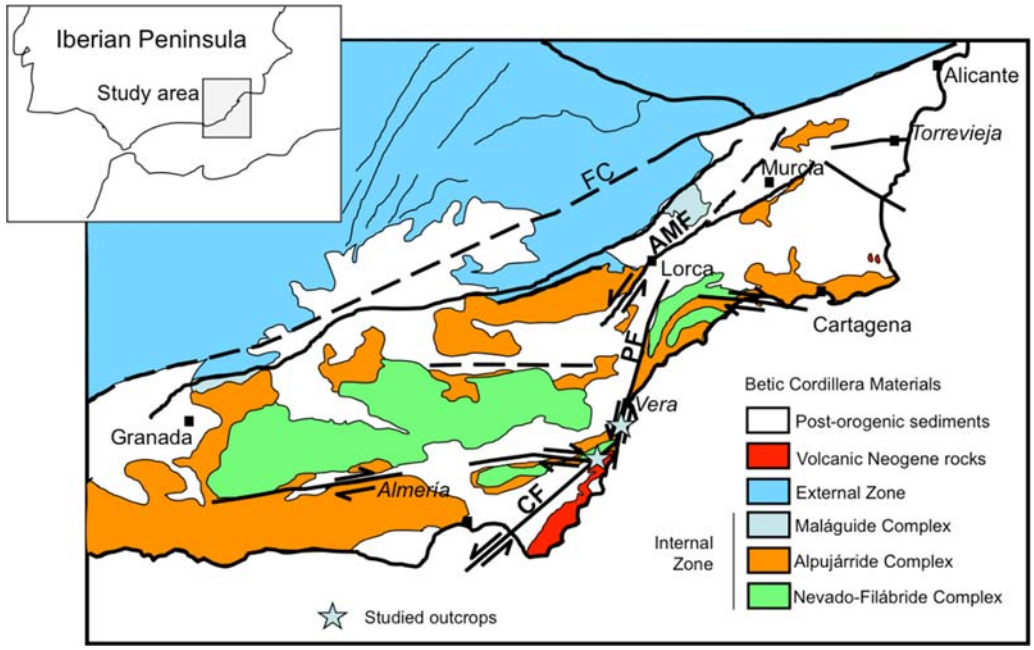


FIG. 1. Geological context of the study area (modified from Gracia *et al*., 2006) indicating the main geological domains of the eastern Betic Cordillera and the main Neogene faults. CRF: Crevillente Fault, AMF: Alhama de Murcia Fault, PF: Palomares Fault, CF: Carboneras Fault.

assemblages and microstructure of the fault rocks and protolith. Phyllosilicate-enrichment of fault rocks can be the result of sedimentary, metamorphic, or hydrothermal processes that occur before, during, or after fault activity. Hydrothermal alteration is especially important in areas with associated volcanic activity. Phyllosilicates are commonly the dominant hydrothermal alteration minerals and their study is therefore important in understanding the alteration conditions, especially with respect to the chemical exchange between quartzitic rocks and hydrothermal fluids. Moreover, hydrothermal cementation with crystallization of carbonate or quartz commonly takes place in fault rocks and can lead to a significant strengthening (*e.g.* Karner *et al*., 1997; Olsen *et al*., 1998; Muhuri *et al*., 2003).

The effects of post-faulting alteration limit inferences about fault behaviour that can be drawn from exhumed rocks, especially in rocks produced by brittle deformation. Recently exhumed traces of young fault zones exposed in arid climates provide good opportunities to study the influence of phyllosilicates on the deformation style of the rocks and their influence on the seismic behaviour of the faults as a consequence of their lubricant and swelling properties (Wu *et al.*, 1975; Chester *et al.*, 1993; Morrow *et al.*, 2000; Warr & Cox, 2001; Bedrosian *et al.*, 2004; Schleicher *et al*., 2006).

On the other hand, the behaviour of aquifers in regions affected by active faults is influenced by the geological processes associated with the nucleation and propagation of seismic movements that occur in these zones (Faulkner *et al*., 2009). Movement associated with active fault zones produces hydrological variations in the surrounding groundwater, such as increases in stream flow from wells (Bolognesi, 1997), changes in the regional thermal transport (higher temperatures to limit hydrothermalism (20°C), and variations in the aquifer behaviour. All these processes commonly produce mixing of water with deep and surficial origins that modify physical-chemical groundwater parameters, such as changes in water-outlet temperature and chemical composition (*e.g.* incorporation of abnormal boron traces) (Montgomery & Manga, 2003; Yuce, 2007; Brumm *et al*., 2009; Manga & Rowland, 2009; Italiano *et al*., 2010; Hernández-Puentes *et al*., 2015).

This paper presents new mineralogical, petrological, hydrochemical and geochemical observations of the presence of phyllosilicate and cementation minerals in fault rocks. The role of the fluid–rock interaction

https://doi.org/10.1180/claymin.2015.050.5.06 Published online by Cambridge University Press

processes in their origin and the influence of these minerals on the mechanical properties of quartzitic rocks in fault areas controlling the general seismic behaviour of fault zones are discussed. For this purpose the Carboneras and Palomares fault zones (Betic Cordillera, SE Spain), which are located in an arid region, with outcrops of quartzitic rocks in slaty and volcanic rocks, have been selected.

## GEOLOGICAL CONTEXT AND MATERIALS

The Betic Cordillera is an ENE–WSW–trending fold-and-thrust belt composed of the External Zone, Mesozoic to Tertiary rocks corresponding to the Iberian Plate palaeomargin, lain down on top of the Variscan basement; and the Internal Zone or Alboran domain, consisting of a thrust stack of metamorphic complexes in SE Spain (Sanz de Galdeano, 1990). Superimposed on the structure above, Neogene to Quaternary sediments fill the intramontane basins, limited by E–W and NE–SW faults (Montenat & Ott D'Estevou, 1995). Moreover, Middle Miocene to Pleistocene calc-alkaline to K-rich volcanic rocks crop out in the Cabo de Gata area (Duggen *et al*., 2004).

The Neogene and Quaternary faulting activity in the southeastern Iberian Margin is dominated by a large NE–SW left-lateral strike-slip fault system including the Palomares and Carboneras faults (Fig. 1). The fault system is, by far, the longest continuous fault mapped in the Betic Cordillera and, therefore, would seem to be a good candidate to generate large-magnitude earthquakes (Gracia *et al*., 2006). Surprisingly, however, seismicity in the area is mainly characterized by low- to moderate-magnitude events. Nevertheless, occasional large destructive earthquakes have occurred in the region and therefore comprise significant earthquake and tsunami hazards to the coasts of Spain and North Africa (IGN, 2001; Masana *et al*., 2004).

Due to the internal architecture of the fault zone, shear lenses of Miocene and Pliocene sediments, including marls and quartz-rich rock sequences, are juxtaposed to the predominant slaty gouges of the Alpine basement. Microcataclasites and gouges of the quartz-rich post-orogenic sediments also occur as cm- to m-scale bands, allowing a comparison between the fault-damaged materials and their protoliths (Fig. 2a). Red, yellow, and white quartz-rich rocks and their respective cataclasites can be identified and are the subject of this research. Polished and striated surfaces are very common in these rocks (Fig. 2b).

Then, damaged rocks and their respective protoliths discussed here were collected from two areas: (1) The Rambla de la Granatilla valley near the locality of Sopalmo in the Carboneras fault area; and (2) the fault lenses cropping out between the localities of Mojacar and Garrucha in the Palomares fault area. Both areas expose sections for a thickness of nearly 200 m of fault gouges and protoliths showing a complex arrangement of shear lenses of the different fault-rock types studied here. These sections were investigated in detail and 42 samples of the different fault rocks were collected for mineralogical, petrological and geochemical characterization.

In order to analyse the composition of groundwater in fault zones within these two study areas, two field sampling campaigns (July 2008 and June 2013) were carried out, taking samples from seven sampling sites including wells and springs.


FIG. 2. (a) Panoramic view of the shear lenses of slaty gouges of the Alpine basement and sediments of Miocene and Pliocene age. (b) Detail of a fault surface in a yellow quartz-rich rock.

https://doi.org/10.1180/claymin.2015.050.5.06 Published online by Cambridge University Press

## ANALYTICAL METHODS

Rock samples were studied by optical microscopy, X-ray diffraction (XRD), scanning electron microscopy (SEM) with EDX microanalyser, electron backscattered diffraction (EBSD), electron probe microanalyser (EMPA), and high-resolution and analytical electron microscopy (HRTEM/AEM).

The XRD data were obtained from powders and orientated aggregates (whole-rock samples and <2 μm fraction) with a Siemens D-5000 diffractometer equipped with a θ/2θ goniometer and using CuKα radiation with a voltage of 35 kV and a current of 25 mA (University of Jaén). Dry samples were scanned from 2° to 70°2θ and glycolated samples were scanned from 2° to 30°2θ to corroborate the identification of expandable clays.

The SEM study was made on polished thin sections with two different microscopes: (1) a Jeol 5800 electron microscope equipped with a Link Isis microanalyser (University of Jaén); and (2) a Zeiss DSM-950 electron microscope equipped with a Link QX2000 microanalyser (University of Granada). Observations were made using backscattered electron images (BSE) in the atomic number contrast mode. The following compounds were used as calibration standards: albite, orthoclase, periclase, wollastonite and synthetic oxides ($Al_2O_3$, $Fe_2O_3$ and $MnTiO_3$). Analytical data were ZAF corrected. The chemical compositions of micas were calculated on the basis of 22 negative charges ($O_{10}(OH)_2$) and chlorite composition were calculated on the basis of 28 negative charges.

A Camebax SX-50 EMPA (University of Granada) provided quantitative chemical analyses of quartz. Count times averaged ~30 s for major elements, while count times for trace elements were increased to reduce detection limits. Detection limits for these analyses averaged 0.01 wt.% (100 ppm) for all elements. The EBSD data were obtained using a CamScan X500 Crystal Probe SEM fitted with a field emission gun and a FASTRACK stage and a Philips XL30 SEM fitted with a tungsten filament (University of Liverpool).

The HRTEM study was carried out with a Philips CM20 (STEM) operating at 200 kV (University of Granada). The point-to-point resolution was 0.27 nm in the TEM mode and 5 nm in the STEM mode. Chemical analyses of particles on carbon-coated Cu grids were obtained in the STEM mode with an EDAX microanalysis system. A (20 nm × 100 nm) scanning area with the long axis orientated parallel to phyllosilicate packets and a 5 nm beam diameter was used for each analysis. Counting times were 100 s except for Na and K, which were analysed using counting times of 15 s to minimize alkali-loss problems as short counting times improve reproducibility for K and Na (Nieto *et al.,* 1996). Albite, olivine, biotite, spessartine, muscovite, chlorite and titanite were used to obtain k-factors for transformation of intensity ratios to concentration ratios according to the approximation of Cliff & Lorimer (1975).

Whole-rock analyses of the major elements of selected samples were carried out using X-ray fluorescence (XRF) and inductively coupled plasma-mass spectrometry (ICP-MS) at Activation Laboratories Ltd. (Ontario, Canada). To prevent a single analysis from skewing the results, we examined wherever possible variations of mean values of each component from averaged analyses of protolith and damaged samples.

The composition of groundwater in the fault zone within the study area, was analysed by means of water samples taken from seven sampling points, including wells and springs and in two different field campaigns (2008 and 2013). Majority components, boron (B) and tritium ($^3H$) were analysed in these samples. The physico-chemical parameters determined using a Hanna Instruments multiparameter water-quality sensor (HI 9828) *in situ* were: electrical conductivity for a standard temperature of 25°C (E.C. (μS/cm), with sensitivity ±1 μS/cm), total dissolved solids (TDS (ppm), ±1 mg/L), pH (±0.02), and temperature ($T$) (°C, ±0.15°C). The alkalinity was also measured through volumetric determination. The samples were kept in ice boxes and stored in the laboratory at 4°C for further analysis.

The major elements were obtained through conductivity detection in an ion chromatograph model Metrohm 850 Professional (relative errors of analysis are ±1% for major anions and cations) (University of Jaén). The analysis of metals and trace elements were performed using an Agilent Model 7500 ICP-mass spectrometer at the University of Granada, the errors being <5% RSD. Tritium ($^3H$) was determined using a Beckman LS6500 scintillation counter (liquid scintillation Gold LLT, Perkin Helmer) in 'low level' over 100 min cycles for every sample with uncertainties within ±5%. The boron content was measured at the Scada S.A. Laboratory (Granada-Spain) with an UV-170 spectrophotometer using the azomethine colorimetric method, the relative errors being between ±0.28 and 0.42%.

The *AquaChem* software package (Schlumberger Water Services) and *Phreeqc* for Windows (USGS) were used to process and study the hydrochemical data.

https://doi.org/10.1180/claymin.2015.050.5.06 Published online by Cambridge University Press

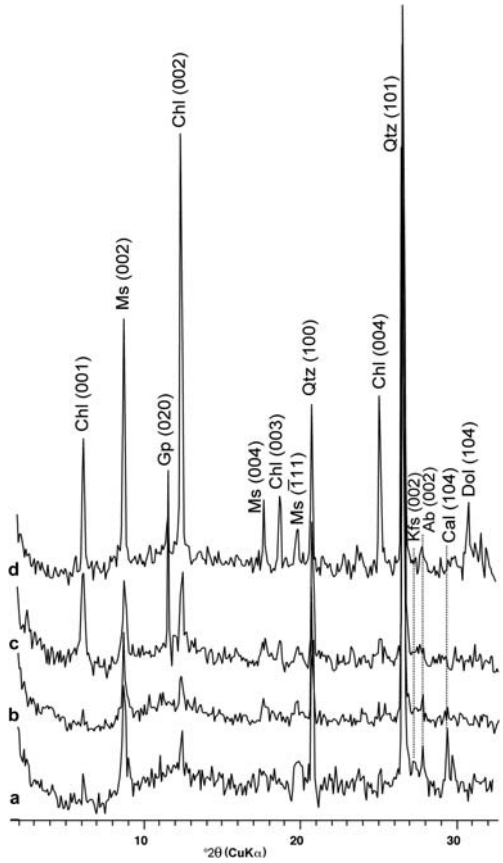


FIG. 3. XRD patterns of air-dried materials: (a) undamaged red quartz-rich rock; (b) undamaged yellow, quartz-rich rock; (c) damaged yellow, quartz-rich rock; (d) damaged white, quartz-rich rock. Mineral abbreviations according to Kretz (1983): Chl = chlorite, Dol = dolomite, Gp = gypsum, Kfs = K-feldspar, Ms = muscovite, Qtz = quartz, Ab = Albite, Cal = Calcite.

## MINERALOGY AND PETROGRAPHY

### *Protoliths*

The predominant mineral assemblage of the undamaged samples comprises quartz and mica, with small amounts of chlorite, feldspars and calcite (Fig. 3). Chlorite was identified by the 001 spacing at 14.2 Å, which remains unaffected by ethylene-glycol saturation or heating at 550°C. The XRD patterns also show a narrow 001 peak at 10 Å which indicates the presence of mica. The intensity of this peak does not increase significantly after heating and ethylene glycol solvation, suggesting the absence of expandable layers. Optical and

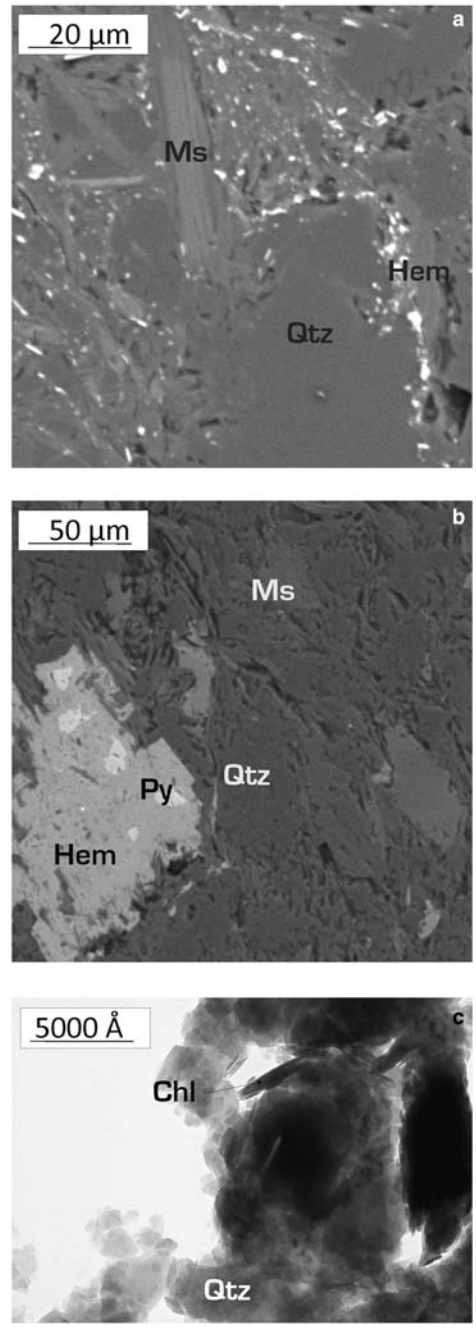


FIG. 4. Photomicrographs of the fabric of the undamaged rocks: (a) BSE image of a red, quartz-rich rock; (b) BSE image of a yellow, quartz-rich rock. (c) TEM bright field of a white, quartz-rich rock. Mineral abbreviations according to Kretz (1983): Chl = chlorite, Hem = hematite, Ms = muscovite, Py = Pyrite, Qtz = quartz.

https://doi.org/10.1180/claymin.2015.050.5.06 Published online by Cambridge University Press

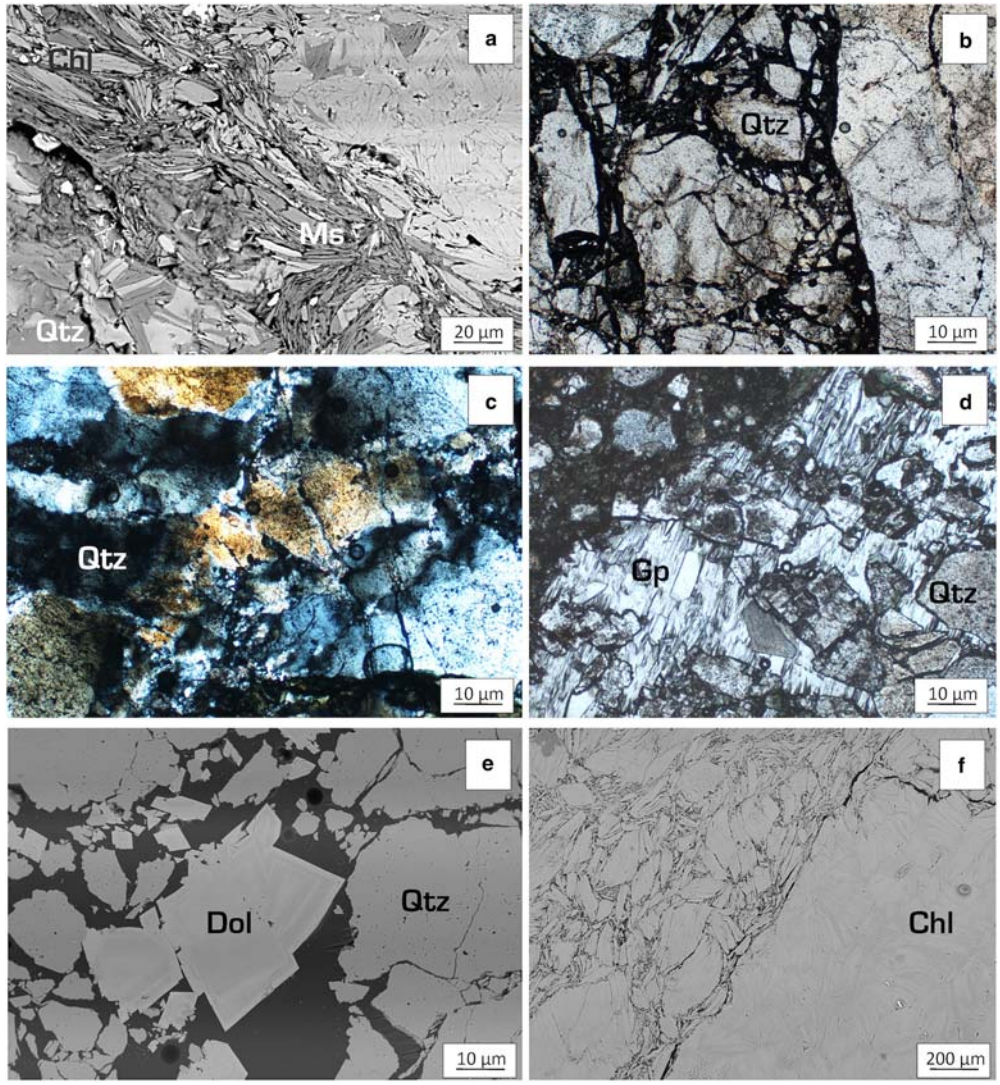


FIG. 5. Photomicrographs of the fabric of the damaged rocks: (a) BSE image of a white, quartz-rich rock developing a highly foliated phyllosilicate-rich band; (b, c) optical photomicrographs of a white, quartz-rich rock, showing the effects of fault deformation on quartz grains; (d) optical photomicrograph of gypsum crystals in a cross-cutting vein of a white quartz-rich rock; (e) BSE image of dolomite crystals in a cross-cutting vein of a white, quartz-rich rock; and (f) BSE image of a phyllosilicate patch in an undeformed lens of a white, quartz-rich rock. Mineral abbreviations according to Kretz (1983): Chl = chlorite, Dol = dolomite, Gp = gypsum, Ms = muscovite, Qtz = quartz.

electron microscope petrography reveals that all the quartz-rich rocks are poorly sorted and fine- to medium-grained. Detrital grains of quartz are surrounded by mica (Fig. 4a,b) and chlorite (Fig. 4c), the alignment of which defines weak slaty cleavage. Quartz grains commonly make up >70% of the rock volume. Red quartz-rich rocks contain abundant hematite (15%) (Fig. 4a), whereas yellow and white quartz-rich rocks contain minor pyrite altered to hematite (Fig. 4b), apatite, and rutile.

### *Damaged rocks*

Although the mineral assemblage is controlled strongly by the protolith, the fault-damaged quartz-rich

https://doi.org/10.1180/claymin.2015.050.5.06 Published online by Cambridge University Press

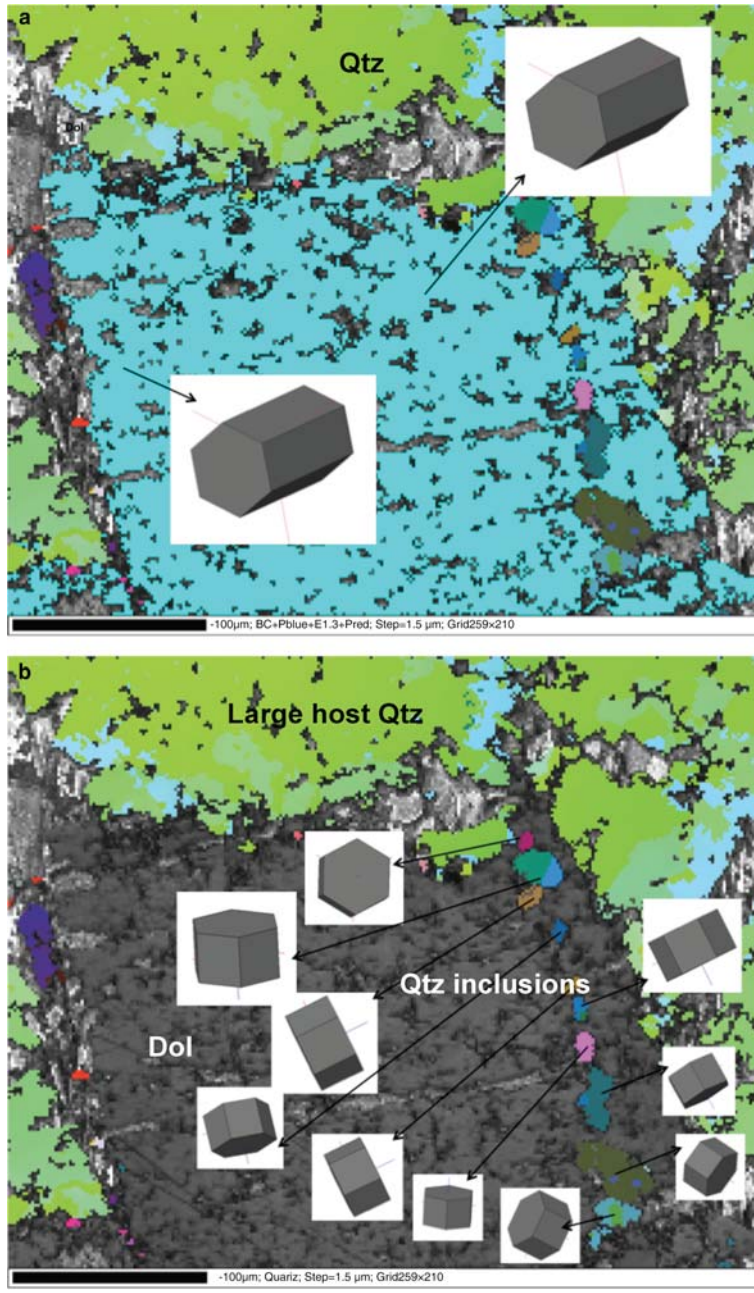


FIG. 6. EBSD texture component maps and representations of crystal orientations: (a) dolomite crystal orientation; and (b) large host quartz grains and small quartz grains included in dolomite xenoblasts.

rocks are enriched in phyllosilicates, in particular with abundant chlorite (Fig. 3). The intensity and position of the chlorite and mica peaks remain unaffected by heating and ethylene glycol solvation, suggesting the absence of expandable layers. Strongly damaged samples are also characterized by the presence of dolomite and gypsum.

The microscopy study reveals a heterogeneous distribution of deformation in the fault zone rocks

https://doi.org/10.1180/claymin.2015.050.5.06 Published online by Cambridge University Press

(Fig. 5). There are numerous, individually recognizable high-strain zones, with well-developed gouge material. Among them are less strained lenses consisting of variably damaged protoliths. The deformation between the lenses is highly localized, developing highly foliated phyllosilicate-rich bands due to the presence of fine-sized aligned chlorite and mica crystals (Fig. 5a). Fault deformation also produces grain-size reduction of quartz grains by brittle fracturing (intragranular and intergranular cracking) and grain-boundary sliding (Fig. 5b). Isolated quartz clasts can exhibit intragranular fracturing, as well as fragment rotation, and in some cases faint signs of crystal plasticity such as undulose extinction (Fig. 5c). It is common to find dolomite and/or gypsum in cross-cutting veins as well as in re-cemented microcataclasite areas within the rock (Fig. 5d,e).

The EBSD data indicate that large dolomite crystals show no evidence of internal misorientation and their crystallographic orientations are not scattered (Fig. 6a). Texture component maps and pole figures of the quartz grains reveal strong internal misorientation in the large host quartz grains (Fig. 6b). Their crystallographic axis has been rotated around the *c* axis. On the other hand, small quartz grains do not show internal misorientation, with a general slight orientation among them according to the dolomite vein direction (Fig. 6b).

In some undamaged lenses of the cataclastic rocks, variably sized patches of phyllosilicates contain randomly orientated stacks of chlorite and mica (Fig. 5f). Back-scattered electron (BSE) images indicate that the stacks consist of two intergrown compositional types of chlorite.

## MINERAL COMPOSITIONS

Analyses by SEM-EDX showed that it is mainly detrital Na-K micas which define the weak slaty cleavage of the rocks and these are characterized by very small Fe and Mg contents (commonly <0.1 a.p.f.u.). Some Na-poor micas with Fe + Mg contents of >0.2 a.p.f.u. can also be identified surrounding the quartz clasts and in the randomly oriented patches in the undamaged lenses of the faulted samples (Table 1). The chemical composition of the fine-grained muscovites in the highly foliated bands of phyllosilicates, where fault deformation is localized, corresponds to the same compositional varieties described previously (Table 2). In all cases, analyses are characterized by a very small deficit in the interlayer charge indicating that both the original and fault-damaged dioctahedral micas are well crystallized.

Systematic differences in the chemical composition between the two types of chlorite identified in the BSE images from the randomly oriented patches of the faulted samples is revealed (Table 3): bright chlorite is Fe-rich (Fe/Mg > 1.15) and Al-rich (Si/Al < 0.90), whereas dark chlorite corresponds to a Mg-rich variety (Fe/Mg < 1.00) with smaller Al contents and greater Si contents than their Fe-rich counterparts (Si/Al > 0.90). These compositional differences have also been observed in the deformed chlorite of the localized deformation bands (Table 4).

Analysis by EPMA allows identification of chemical variations of trace elements in different quartz generations. Samples were analysed for Al (detection limit, d.l. = 0.007%), Zn (d.l. = 0.005%), Pb (d.l. = 0.006%),

TABLE 1. Representative EDS-SEM microanalyses of micas normalized to $O_{10}(OH)_2$ in the protoliths.

| | Si | $^{IV}$Al | $^{VI}$Al | Fe | Mg | Ti | $^{VI}\sum$. | K | Na | Ca | $\sum$inter. |
|---|---|---|---|---|---|---|---|---|---|---|---|
| 1 | 3.12 | 0.88 | 1.94 | 0.06 | 0.03 | 0.02 | 2.05 | 0.34 | 0.47 | 0.00 | 0.81 |
| 2 | 3.11 | 0.89 | 1.93 | 0.08 | 0.04 | 0.00 | 2.05 | 0.45 | 0.39 | 0.01 | 0.85 |
| 3 | 3.09 | 0.91 | 1.90 | 0.06 | 0.08 | 0.01 | 2.05 | 0.47 | 0.39 | 0.01 | 0.88 |
| 4 | 3.05 | 0.95 | 1.94 | 0.07 | 0.04 | 0.01 | 2.05 | 0.49 | 0.41 | 0.00 | 0.90 |
| 5 | 3.08 | 0.92 | 1.83 | 0.14 | 0.07 | 0.01 | 2.05 | 0.75 | 0.20 | 0.01 | 0.96 |
| 6 | 3.13 | 0.87 | 1.64 | 0.29 | 0.15 | 0.02 | 2.09 | 1.00 | 0.01 | 0.00 | 1.01 |
| 7 | 3.09 | 0.91 | 1.81 | 0.14 | 0.10 | 0.03 | 2.08 | 0.82 | 0.07 | 0.00 | 0.89 |
| 8 | 3.03 | 0.97 | 1.84 | 0.11 | 0.10 | 0.03 | 2.08 | 0.84 | 0.09 | 0.00 | 0.93 |
| 9 | 3.05 | 0.95 | 1.86 | 0.15 | 0.09 | 0.00 | 2.11 | 0.78 | 0.10 | 0.00 | 0.87 |
| 10 | 3.06 | 0.94 | 1.87 | 0.16 | 0.04 | 0.00 | 2.07 | 0.82 | 0.11 | 0.00 | 0.94 |

1–4: detrital Na-K micas; 5–6: micas from red quartz-rich rocks; 7–10: micas from randomly oriented phyllosilicate patches in undamaged bands of white quartz-rich faulted rocks.

https://doi.org/10.1180/claymin.2015.050.5.06 Published online by Cambridge University Press

TABLE 2. Representative analyses of micas normalized to $O_{10}(OH)_2$ in the damaged quartz-rich rocks of the fault zone.

| | Si | $^{IV}$Al | $^{VI}$Al | Fe | Mg | Ti | $^{VI}\sum$ | K | Na | Ca | $\sum$inter. |
|---|---|---|---|---|---|---|---|---|---|---|---|
| 1* | 3.14 | 0.86 | 1.94 | 0.06 | 0.02 | 0.02 | 2.04 | 0.34 | 0.46 | 0.00 | 0.80 |
| 2* | 3.13 | 0.87 | 1.93 | 0.07 | 0.04 | 0.00 | 2.04 | 0.45 | 0.39 | 0.01 | 0.85 |
| 3* | 3.12 | 0.88 | 1.95 | 0.05 | 0.02 | 0.02 | 2.04 | 0.35 | 0.48 | 0.00 | 0.82 |
| 4* | 3.12 | 0.88 | 1.93 | 0.07 | 0.03 | 0.00 | 2.04 | 0.45 | 0.40 | 0.01 | 0.85 |
| 5* | 3.12 | 0.88 | 1.95 | 0.06 | 0.02 | 0.02 | 2.04 | 0.34 | 0.47 | 0.00 | 0.81 |
| 6* | 3.12 | 0.88 | 1.93 | 0.07 | 0.04 | 0.00 | 2.05 | 0.44 | 0.39 | 0.01 | 0.84 |
| 7* | 3.14 | 0.86 | 1.60 | 0.29 | 0.15 | 0.02 | 2.06 | 1.09 | 0.01 | 0.00 | 1.11 |
| 8* | 3.21 | 0.79 | 1.59 | 0.28 | 0.16 | 0.02 | 2.05 | 1.03 | 0.01 | 0.00 | 1.04 |
| 9* | 3.17 | 0.83 | 1.59 | 0.30 | 0.17 | 0.02 | 2.08 | 1.03 | 0.01 | 0.00 | 1.05 |
| 10* | 3.11 | 0.89 | 1.63 | 0.29 | 0.18 | 0.02 | 2.12 | 0.94 | 0.02 | 0.00 | 0.96 |
| 11** | 3.09 | 0.91 | 1.82 | 0.15 | 0.09 | 0.02 | 2.08 | 0.81 | 0.10 | 0.00 | 0.91 |
| 12** | 3.11 | 0.89 | 1.75 | 0.15 | 0.13 | 0.04 | 2.06 | 0.89 | 0.04 | 0.00 | 0.93 |

1–6: Na-K micas from yellow quartz-rich rocks; 7–10: K-rich micas from red quartz-rich rocks; 11–12. K rich micas from damaged phyllosilicate patches in white quartz-rich faulted rocks.
*AEM microanalyses.
**EDS-SEM microanalyses.

Ti (d.l. = 0.005%), Fe (d.l. = 0.004%), Mg (d.l. = 0.006%), S (d.l. = 0.005%), As (d.l. = 0.008%) and Sb (d.l. = 0.004%) (Table 5). Aluminium is the most abundant trace element and is significantly more abundant in the small quartz grains included in dolomite veins (0.432–0.731 wt.%) than in the large host quartz grains damaged by the effect of the fault, where Al was typically below detection. Significant amounts of As and Sb where also detected in both type of quartz grains. The Sb and As contents reached 0.091 and 0.185 wt.%, respectively, in small quartz grains included in veins, whereas in host quartz grains they are generally below

TABLE 3. Representative analyses of chlorite normalized to $O_{10}(OH)_8$ in the protoliths.

| | Si | $^{IV}$Al | $^{VI}$Al | Fe | Mg | Mn | Ti | $^{VI}\sum$ |
|---|---|---|---|---|---|---|---|---|
| 1* | 2.50 | 1.50 | 1.45 | 2.69 | 1.85 | 0.03 | 0.00 | 6.02 |
| 2* | 2.70 | 1.30 | 1.30 | 2.04 | 2.66 | 0.00 | 0.00 | 6.00 |
| 3* | 2.52 | 1.48 | 1.45 | 2.66 | 1.87 | 0.03 | 0.00 | 6.01 |
| 4* | 2.56 | 1.44 | 1.44 | 2.61 | 1.92 | 0.03 | 0.00 | 6.00 |
| 5* | 2.71 | 1.29 | 1.29 | 2.07 | 2.63 | 0.00 | 0.00 | 6.00 |
| 6* | 2.72 | 1.28 | 1.29 | 2.08 | 2.62 | 0.00 | 0.00 | 6.00 |
| 7** | 2.49 | 1.51 | 1.47 | 2.72 | 1.80 | 0.03 | 0.00 | 6.02 |
| 8** | 2.50 | 1.50 | 1.52 | 2.61 | 1.87 | 0.00 | 0.00 | 5.99 |
| 9** | 2.53 | 1.47 | 1.46 | 2.46 | 2.06 | 0.02 | 0.00 | 6.00 |
| 10** | 2.63 | 1.37 | 1.38 | 2.25 | 2.37 | 0.00 | 0.00 | 6.00 |
| 11** | 2.60 | 1.40 | 1.36 | 2.20 | 2.42 | 0.04 | 0.00 | 6.02 |
| 12** | 2.66 | 1.34 | 1.31 | 1.99 | 2.71 | 0.00 | 0.00 | 6.01 |

1–2: chlorite from yellow quartz-rich rocks; 3–6: chlorite from red quartz-rich rocks; 9–12: chlorite from randomly oriented phyllosilicate patches in undamaged bands of white quartz-rich faulted rocks.
*AEM microanalyses.
**EDS-SEM microanalyses.

https://doi.org/10.1180/claymin.2015.050.5.06 Published online by Cambridge University Press

TABLE 4. Representative analyses of chlorite normalized to $O_{10}(OH)_8$ in the damaged quartz-rich rocks of the fault zone.

| | Si | $^{IV}$Al | $^{VI}$Al | Fe | Mg | Mn | Ti | $^{VI}\sum$ |
|---|---|---|---|---|---|---|---|---|
| 1* | 2.54 | 1.46 | 1.44 | 2.64 | 1.89 | 0.03 | 0.00 | 6.01 |
| 2* | 2.69 | 1.31 | 1.31 | 2.03 | 2.67 | 0.00 | 0.00 | 6.00 |
| 3* | 2.58 | 1.42 | 1.45 | 2.58 | 1.93 | 0.03 | 0.00 | 5.99 |
| 4* | 2.68 | 1.32 | 1.31 | 2.02 | 2.68 | 0.00 | 0.00 | 6.01 |
| 5* | 2.49 | 1.51 | 1.46 | 2.71 | 1.82 | 0.03 | 0.00 | 6.03 |
| 6* | 2.67 | 1.33 | 1.31 | 2.01 | 2.69 | 0.00 | 0.00 | 6.01 |
| 7* | 2.60 | 1.40 | 1.45 | 2.55 | 1.95 | 0.03 | 0.00 | 5.98 |
| 8* | 2.70 | 1.30 | 1.30 | 2.06 | 2.64 | 0.00 | 0.00 | 6.00 |
| 9** | 2.48 | 1.52 | 1.49 | 2.63 | 1.86 | 0.03 | 0.00 | 6.01 |
| 10** | 2.55 | 1.45 | 1.43 | 2.63 | 1.96 | 0.00 | 0.00 | 6.01 |
| 11** | 2.60 | 1.40 | 1.38 | 2.41 | 2.22 | 0.00 | 0.00 | 6.01 |
| 12** | 2.73 | 1.27 | 1.30 | 2.38 | 2.28 | 0.03 | 0.00 | 5.99 |
| 13** | 2.69 | 1.31 | 1.29 | 2.18 | 2.52 | 0.03 | 0.00 | 6.01 |
| 14** | 2.67 | 1.33 | 1.32 | 2.06 | 2.60 | 0.03 | 0.00 | 6.00 |

1–4: chlorite from yellow damaged quartz-rich rocks; 5–8: chlorite from damaged red quartz-rich rocks; 9–14: chlorite from damaged phyllosilicate patches in white quartz-rich faulted rocks.
*AEM microanalyses.
**EDS-SEM microanalyses.

detection. Other trace metals are present in only a few analyses and in low concentrations.

## HYDROCHEMICAL DATA

The results of the chemical analyses of the two field sampling campaigns for groundwaters are listed in Table 6. In general, significant differences between them were not observed. Samples from aquifers affected by the faults in this area are characterized by medium to high electrical conductivity. Conductivities of ~680 μS/cm were detected in sampling points from fault lenses cropping out near Mojacar (*i.e.* the Mora Spring), which correspond to carbonate rocks from

TABLE 5. Representative WDS analyses of quartz in the damaged quartz-rich rocks of the fault zone.

| | $SiO_2$ | Al | Zn | Pb | Ti | Fe | Mg | S | As | Sb | Total |
|---|---|---|---|---|---|---|---|---|---|---|---|
| 1 | 99.455 | 0.446 | – | – | – | 0.004 | – | 0.025 | 0.081 | 0.027 | 99.455 |
| 2 | 99.155 | 0.715 | – | 0.010 | – | 0.010 | 0.008 | 0.031 | 0,185 | 0.091 | 99.155 |
| 3 | 99.291 | 0.673 | – | – | – | – | – | – | 0.126 | 0.064 | 99.291 |
| 4 | 99.640 | 0.638 | – | – | – | – | – | 0.012 | 0.079 | 0.031 | 99.640 |
| 5 | 99.442 | 0.906 | – | 0.011 | – | – | – | 0.011 | 0.098 | 0.052 | 99.442 |
| 6 | 99.677 | – | – | 0.010 | – | 0.006 | – | – | – | – | 99.677 |
| 7 | 98.756 | 0.010 | 0.010 | – | – | – | – | 0.005 | – | – | 98.756 |
| 8 | 93.297 | – | – | – | – | – | 0.041 | – | – | – | 93.297 |
| 9 | 98.915 | – | – | – | – | – | 0.011 | 0.006 | – | 0.004 | 98.915 |
| 10 | 96.988 | 0.008 | 0.007 | – | – | – | – | 0.009 | – | – | 96.977 |

–: below detection limits; 1–5: small quartz grains included in dolomite veins; 6–10: large host quartz grains damaged by the effect of the fault.

https://doi.org/10.1180/claymin.2015.050.5.06 Published online by Cambridge University Press

TABLE 6. Physical-chemical parameters and saturation indexes of groundwaters from the fault-zone aquifers.

| | Water name | EC | pH | T | $Na^+$ | $K^+$ | $Ca^{2+}$ | $Mg^{2+}$ | $Cl^-$ | $HCO_3^-$ | B | $^3H$ |
|---|---|---|---|---|---|---|---|---|---|---|---|---|
| 1 | Mora S.1 | 739 | 6.8 | 20 | 33.6 | 6.3 | 63.7 | 33.5 | 52.6 | 167.8 | | |
| 2 | Mora S.2 | 681 | 7.5 | 21 | 42.2 | 7.2 | 67.9 | 37.6 | 51.2 | 183.1 | 0.1 | 3.38 |
| 3 | Sopalmo S.1 | 1907 | 7.2 | 22 | 262 | 7.9 | 82.9 | 68.2 | 284 | 518.7 | | |
| 4 | Sopalmo S.2 | 1940 | 7.2 | 25 | 277 | 8.3 | 86.7 | 76.7 | 256 | 500.4 | 0.36 | 0.65 |
| 5 | Sopalmo G.1 | 2730 | 7.0 | 22 | 262 | 1.9 | 185 | 150 | 568 | 524.7 | | |
| 6 | Sopalmo G.2 | 2970 | 6.9 | 22 | 288 | 2.5 | 217 | 185.1 | 553.2 | 561.4 | 0.42 | 2.26 |
| 7 | Sopalmo W. | 6222 | 7.7 | 26 | 819 | 7.2 | 224 | 276 | 1794 | 610.2 | 0.46 | 0.70 |

Spring (S.); Gallery (G.); Well (W.).
EC: µS/cm; *T*: °C.
Concentrations of major elements and boron expressed in mg/L. Concentrations of tritium expressed in TU.

Sierra Cabrera, with $HCO_3^-$-$SO_4^{2-}$-$Ca^{2+}$-$Mg^{2+}$ water facies and a low degree of ion enrichment (~15 meq/L). This groundwater is undersaturated in evaporite minerals (gypsum and halite) and it is slightly undersaturated for carbonates (calcite and dolomite) allowing for potential dissolution of these minerals (Fig. 7). Dissolution or precipitation of clay minerals in this groundwater is not observed.

On the other hand, waters from the Sopalmo-Rambla de la Granatilla area show conductivities from 1940 µS/cm to 6220 µS/cm, which are related to mixing of waters rich in $Cl^-$, with some influence of $SO_4^{2+}$ and $HCO_3^-$, high $Na^+$- and low $Mg^{2+}$-contents. These groundwaters present medium to high ion-enrichment values (from 18 to 70 meq/L) and they demonstrate saturation or are much closer to equilibrium with carbonates (calcite and dolomite). However, these groundwaters are undersaturated with respect to evaporite minerals (gypsum and halite). Such concentrations are indicative of water from the sedimentary marine formations either with insufficient amount of evaporite minerals or a short residence time (Singh *et al.,* 2014). Temperatures were generally greater than the limit for hydrothermal activity (~26°C). Abnormally high traces of B were detected in these waters (0.36–0.46 ppm). Tritium analysis results showed values between 0.65 and 3.38 TU. Samples from Sopalmo Spring and Sopalmo Well display tritium contents of <0.8 TU indicating that these waters are sub-modern, *i.e.* recharged prior to 1952 and therefore have a very long and deep underground residence time. However, samples from Mora Spring and Sopalmo Gallery show tritium contents of >0.8 TU, which may indicate a mixing origin between sub-modern and recent recharge (<5–10 y) (Clark & Fritz, 2000; Mook *et al*., 2002; Hernández-Puentes *et al*., 2015).

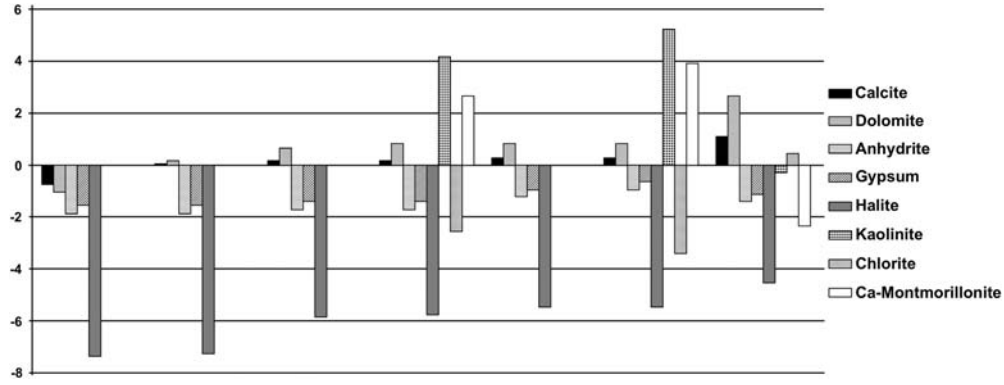


FIG. 7. Saturation index of the Palomares–Carboneras fault zone groundwater samples.

https://doi.org/10.1180/claymin.2015.050.5.06 Published online by Cambridge University Press

TABLE 7. Average whole-rock composition of quartz-rich rocks in the fault zone.

| Analyses | 1 | 2 | 3 | 4 | 5 | 6 |
|---|---|---|---|---|---|---|
| $SiO_2$ | 60.86 | 61.37 | 68.54 | 64.17 | 64.70 | 59.15 |
| $Al_2O_3$ | 17.13 | 15.51 | 13.84 | 13.50 | 15.49 | 9.08 |
| $Fe_2O_3$ | 6.67 | 7.07 | 3.53 | 6.20 | 5.10 | 9.40 |
| MnO | 0.12 | 0.09 | 0.11 | 0.06 | 0.12 | 0.21 |
| MgO | 1.30 | 2.45 | 1.14 | 1.89 | 1.22 | 5.09 |
| CaO | 2.97 | 2.99 | 2.58 | 1.94 | 2.78 | 5.24 |
| $Na_2O$ | 1.20 | 0.93 | 0.84 | 0.75 | 1.02 | 0.20 |
| $K_2O$ | 2.84 | 3.00 | 2.42 | 2.30 | 2.63 | 1.14 |
| $TiO_2$ | 1.00 | 0.80 | 0.91 | 0.82 | 0.96 | 0.40 |
| $P_2O_5$ | 0.16 | 0.14 | 0.13 | 0.11 | 0.15 | 0.06 |
| LOI | 5.50 | 6.13 | 5.06 | 7.27 | 5.28 | 9.43 |
| Sc | 15.00 | 11.00 | 13.00 | 12.00 | 14.00 | 9.00 |
| V | 113.00 | 124.00 | 98.00 | 89.00 | 105.50 | 64.00 |
| Cr | 350.00 | 90.00 | 90.00 | 60.00 | 220.00 | 40.00 |
| Co | 17.00 | 15.00 | 11.00 | 14.00 | 14.00 | 22.00 |
| Ni | 200.00 | 40.00 | 30.00 | 30.00 | 115.00 | 30.00 |
| Cu | 70.00 | 30.00 | <10 | <10 | 40.00 | 20.00 |
| Zn | 90.00 | 100.00 | 50.00 | 90.00 | 70.00 | 70.00 |
| As | <5 | 7.00 | 18.00 | 26.00 | 11.50 | <5 |
| Rb | 144.00 | 137.00 | 140.00 | 122.00 | 142.00 | 42.00 |
| Sr | 139.00 | 114.00 | 102.00 | 103.00 | 120.50 | 74.00 |
| Y | 39.50 | 32.50 | 42.00 | 24.70 | 40.75 | 22.90 |
| Zr | 291.00 | 266.00 | 380.00 | 315.00 | 335.50 | 97.00 |
| Nb | 18.50 | 14.00 | 16.60 | 15.30 | 17.55 | 7.90 |
| Ba | 671.00 | 469.00 | 508.00 | 436.00 | 589.50 | 189.00 |
| La | 49.50 | 43.60 | 49.10 | 43.00 | 49.30 | 18.10 |
| Ce | 101.00 | 85.70 | 95.40 | 82.60 | 98.20 | 35.90 |
| Pr | 11.10 | 9.36 | 10.00 | 8.66 | 10.55 | 3.65 |
| Nd | 37.80 | 33.80 | 37.30 | 28.90 | 37.55 | 13.10 |
| Sm | 7.59 | 7.26 | 8.07 | 5.77 | 7.83 | 2.77 |
| Eu | 1.53 | 1.56 | 1.73 | 1.17 | 1.63 | 0.95 |
| Gd | 6.69 | 6.08 | 7.02 | 4.58 | 6.86 | 3.76 |
| Tb | 1.14 | 0.94 | 1.18 | 0.75 | 1.16 | 0.64 |
| Dy | 6.80 | 5.39 | 6.97 | 4.48 | 6.89 | 3.68 |
| Ho | 1.31 | 1.06 | 1.42 | 0.90 | 1.37 | 0.70 |
| Er | 3.75 | 3.13 | 4.18 | 2.71 | 3.97 | 1.99 |
| Tm | 0.58 | 0.47 | 0.62 | 0.43 | 0.60 | 0.29 |
| Yb | 3.65 | 2.90 | 3.90 | 2.81 | 3.78 | 1.83 |
| Lu | 0.56 | 0.44 | 0.57 | 0.44 | 0.56 | 0.26 |
| W | 3.20 | 2.00 | 5.70 | 6.10 | 4.45 | 1.90 |
| Pb | 16.00 | 25.00 | 10.00 | 7.00 | 13.00 | <5 |
| Th | 15.40 | 13.40 | 15.30 | 13.40 | 15.35 | 6.55 |
| U | 3.26 | 3.14 | 3.67 | 3.23 | 3.47 | 1.21 |

1. Red quartz-rich rocks (average of four samples).
2. Damaged red quartz-rich rocks (average of four samples).
3. Yellow quartz-rich rocks (average of six samples).
4. Damaged yellow quartz-rich rocks(average of five samples).
5. White quartz-rich rocks (average of four samples).
6. Damaged white quartz-rich rocks(average of four samples).
Major elements expressed as wt.% oxide and minor elements expressed in ppm.
LOI: Loss on ignition. Total iron expressed as $Fe_2O_3$.

https://doi.org/10.1180/claymin.2015.050.5.06 Published online by Cambridge University Press

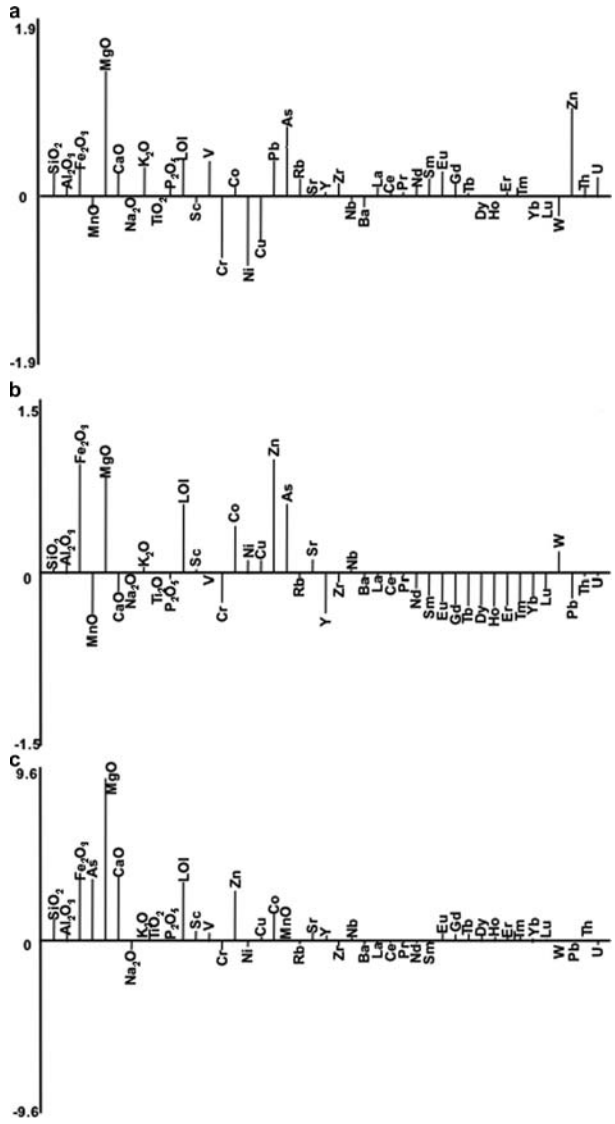


FIG. 8. Histogram of mass variation of components in protoliths *vs.* components in fault-damaged rocks, $(M_i^f - M_i^O)/M_i^O$. $M_i^O$ = mass of component $i$ in the original, fresh rock; $M_i^f$ = mass of component $i$ in the altered rock. (a) Red, quartz-rich rocks; (b) yellow, quartz-rich rocks; and (c) white, quartz-rich rocks.

## WHOLE-ROCK COMPOSITIONS

The results of the chemical analyses of the rocks are listed in Table 7. Geochemical analyses of fault-related rocks allow a comparison of the relative concentration constituents within the fault zone and their respective protoliths. Direct comparisons between chemical analyses of undamaged and damaged rocks, using element concentrations, are not useful, as they do not take into account volume changes that accompany mass transfer. The open-system behaviour of most fault zones with respect to fluids requires a framework to convert variations in chemical composition into units of mass transfer (Gresens, 1967). Grant (1986) modified the equations of Gresens (1967) to develop the isocon method for the calculation of absolute and relative mass or volume changes associated with alteration. This method requires the selection of

https://doi.org/10.1180/claymin.2015.050.5.06 Published online by Cambridge University Press

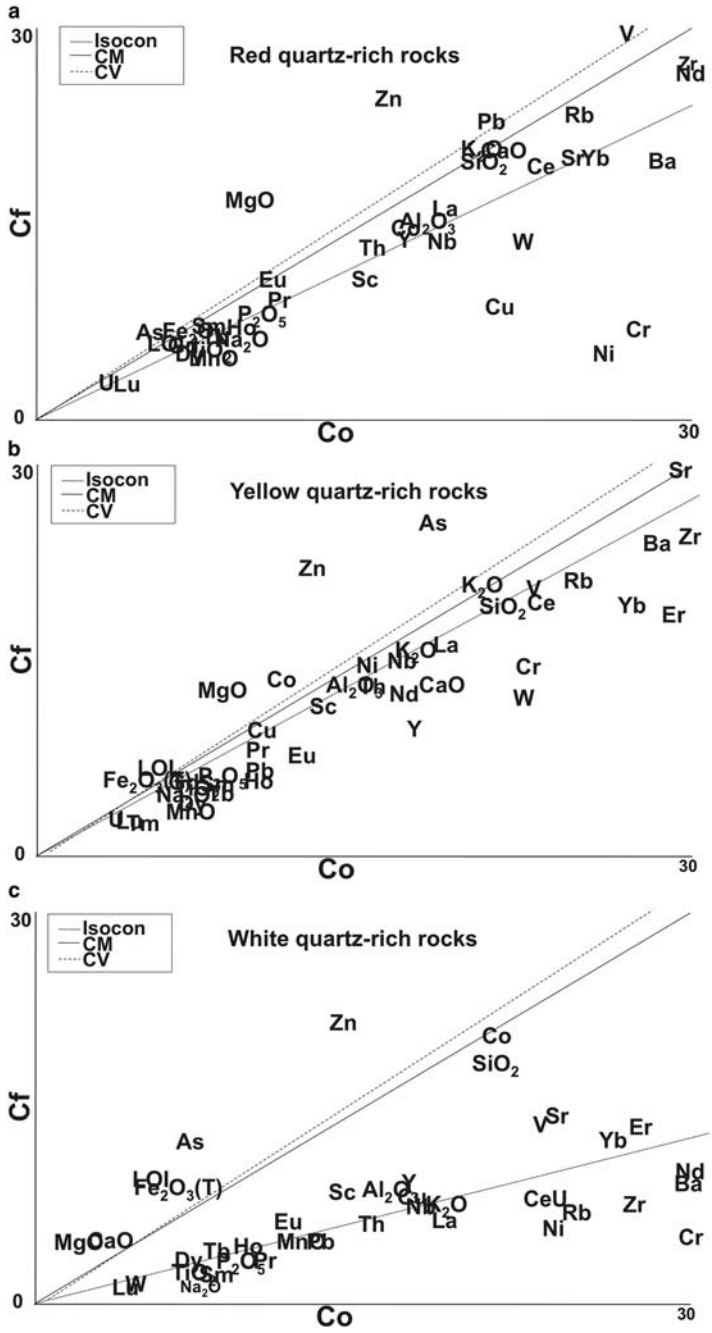


FIG. 9. Isocon plots depicting the variation in bulk-rock chemistry of protoliths *vs.* fault-damaged rocks. $C_i^O$ = concentration of component *i* in the parent rock. $C_i^f$ = concentration of component *i* in the altered rock. (a) Red, quartz-rich rocks; (b) yellow, quartz-rich rocks; (c) white, quartz-rich rocks. Isocon: immobile isocon, CM: isomass isocon, CV: isovolume isocon.

https://doi.org/10.1180/claymin.2015.050.5.06 Published online by Cambridge University Press

immobile elements to define an isocon with which to compare mass gains or loss of elements. Geochemical studies of metasomatized rocks and shear zones suggest the immobility of Ti as well as Mn, Zr, Y and P (Correns, 1978; Dostal *et al*., 1980; Floyd & Winchester, 1983; Winchester & Max, 1984; Sinha *et al*., 1986; O'Hara, 1988; O'Hara & Blackburn, 1989; Glazner & Bartley, 1991). In this study Ti was used as the immobile constituent taking into account these studies and because we did not observe any textural features arguing against this consideration.

The concentration of a component in the altered rock was compared to that in the original through a mass-change term:

$$C_i^A = M^O/M^A(C_i^O + \Delta C_i)$$

where $C_i^A$ = concentration of component $i$ in the altered rock; $M^O$ = mass of the original, fresh rock; $M^A$ = mass of the altered rock; $C_i^O$ = concentration of component $i$ in the parent rock; and $\Delta C_i$ = change in concentration of component $i$.

Examination of variations of elemental concentrations from analyses of protolith and damaged rocks showed significant enrichment in MgO and moderate enrichment in water (represented as loss on ignition, LOI), $Fe_2O_3$, As and Zn in all types of damaged rocks (Fig. 8). CaO displayed moderate enrichment in strongly damaged samples. Moderate rare earth element (*REE*) losses were observed in damaged yellow quartz-rich rocks. Hence, MgO, $Fe_2O_3$, LOI, As, and Zn plot well above the isovolume, isomass and immobile isocon for all types of quartz-rich rocks from the studied fault zones, indicating that these elements are mass enriched in the damaged rocks (Fig. 9).

## DISCUSSION AND CONCLUSIONS

The mineralogy of the fault materials plays an important role in the fault-slip behaviour. Fault materials made of non-phyllosilicate minerals such as quartz and feldspar are frictionally strong and may have the potential for seismic slip, while those made of phyllosilicate minerals are frictionally weak and tend towards stable slip behaviour (Ikari *et al.,* 2011). The Carboneras and Palomares faults offer the opportunity to infer fault-slip processes in quartzo-feldspathic rocks containing localized microdomains enriched in phyllosilicate. Combined XRD, optical and electron microscopy, as well as hydrochemical and geochemical analyses provide the basis for a discussion on the origin of the phyllosilicate enrichment and cementation of the damaged rocks in the fault area and the role of phyllosilicates in the mechanical behaviour of the quartz-rich rocks.

### *The origin of phyllosilicates*

A comparison of the mineralogy and the major-element oxide and trace-element contents for the damaged rocks of the fault area and their respective protoliths suggests that the damaged rocks were altered. The observed chemical and mineralogical changes are probably related to the hydrothermal formation of the phyllosilicates.

Large gains in Mg, Fe and $H_2O$ with the addition of Zn and As is a typical pattern of changes produced by hydrothermal alteration of felsic rocks associated with base-metal mineralizing fluids related to volcanic activity (Benito *et al*., 1998; Humphris *et al*., 1998; Sánchez-España *et al*., 2000; Lackschewitz *et al*., 2004). The most important mineralogical changes in this process are the destruction of the original constituents (hydrolysis of feldspar and dissolution of quartz), with subsequent precipitation of phases such as chlorite. The gain in Fe and Mg during chloritization corresponds to the formation of a Mg-rich chlorite. The presence of Mg-chlorite in hydrothermal systems indicates that the initial fluids were a mixture of hydrothermal fluids and seawater (*e.g.* Humphris *et al*., 1998; Lackschewitz *et al*., 2000).

Near Carboneras, Morales-Ruano *et al*. (2000) identified a stage of propylitic alteration related to the deposit of Palai-Islica, hosted by the volcanic rocks of Cabo de Gata and formed by circulation of fluid, with temperatures between 217 and 315°C. The compositions of chlorites from patches in our study are characterized by high-amesite and low-chlinoclore and sudoite components, which are typical of high-temperature chlorites (Vidal *et al.*, 2005, 2006; Inoue *et al.*, 2009; Bourdelle *et al.*, 2013; Lanari *et al.*, 2014). Unfortunately, due to their large $Fe^{3+}$ contents, which produces anomalously large numbers of octahedral cations, in most cases exceeding the theoretical value of 6, recent approaches using chlorite thermometry cannot be applied quantitatively to these chlorites. In such cases, the application of the thermometric methods produces anomalous temperatures (Vidal *et al.*, 2005, 2006).

Therefore, the replacement of the protoliths of the rocks studied by a chlorite-rich assemblage could be the result of magnesium metasomatism caused by hot hydrothermal fluids, probably influenced by a seawater

https://doi.org/10.1180/claymin.2015.050.5.06 Published online by Cambridge University Press

component associated with the volcanic activity of the Cabo de Gata belt. According to Rutter *et al*. (1986) volcanic heating promoted the alteration of the host rocks. The genesis of chlorite as a secondary mineral in the fault gouge was probably due in part to elevation of the geothermal gradient under the influence of the igneous activity (Rutter *et al.,* 2014).

Chlorite patches are concentrated especially in quartz-rich rocks due to the effect of cracking phases during the increase in fluid pressure related to the hydrothermal processes. Brittle quartz-rich rocks under high fluid pressure conditions undergo several phases of increased permeability approaching failure (attributed to the formation of new microcracks: *e.g.* Brace *et al.*, 1966) than plastic rocks enriched in oriented phyllosilicates. Rock failure, leading to the formation of macroscopic fractures, results in significant increases in permeability (*e.g.* Uehara & Shimamoto, 2004; Walker *et al*., 2013). Hence, pervasive clay-fracture networks in quartz-rich rocks may be related to stages of microcrack formation prior to slip events, coupled with fluid influx and reactions forming clay minerals.

### *Timing of formation and role of phyllosilicates in the mechanical behaviour of the fault zone*

The determination of the timing of formation of phyllosilicates in the damaged rocks of the fault zone is one of the main factors aiding in our understanding of the mechanical role of clays in fault rocks. Damaged quartz-rich rocks from the Carboneras and Palomares fault areas show substantial clay recrystallization with respect to their respective protoliths. The petrographic study of these rocks reveals that undamaged lenses within the fault rocks contain chlorite/mica patches with randomly oriented phyllosilicates. Given that phyllosilicate patches are crossed by shear bands where their components are strongly deformed, it is suggested that the hydrothermal process which produced the phyllosilicate enrichment of the rocks occurred before strike-slip faulting.

Phyllosilicates may weaken faults due to low strength (Wang, 1984). Moreover, their fabrics may influence the permeability structure of fault zones (Morrow *et al*., 1984; Zhang *et al*., 1999; Zhang & Cox, 2000; Faulkner & Rutter, 2001), controlling the mechanism by which fluids are focused along faults to produce elevated fluid pressure that can lead to fault rupture (Sibson, 1990).

The petrographic and compositional characteristics of phyllosilicates in the rocks studied suggest there was limited clay growth during faulting. The absence of significant compositional differences between the fault-damaged phyllosilicates and their original counterparts suggests that, although fluids were present during strike-slip faulting, they were not focused preferentially along the quartz-rich rock fault zone by phyllosilicates, thereby avoiding the development of the syn-kinematic clay-alteration process.

Clays played an important role in the mechanical behaviour of the quartz-rich rocks in the fault zone, however. Deformation is highly localized in chlorite-rich, quartz-rich rocks. The absence of syn-kinematic crystallization of phyllosilicates indicates that, although elevated fluid pressure confined by the clay fabric cannot be considered to have been responsible for the mechanical behaviour of the quartz-rich rocks of the Carboneras and Palomares faults, clay fabrics that developed during deformation dominated the fault-weakening mechanism. The lubricating properties of phyllosilicates in the quartzitic rocks are considered here to be an important factor controlling movement mechanisms, promoting the predominance of creep over seismic stick-slip (Wu *et al*., 1975; Chester *et al*., 1993; Morrow *et al*., 2000; Warr & Cox, 2001; Bedrosian *et al*., 2004), thereby reducing the possibility of larger seismogenic events which nucleate on localized fault planes within quartzitic rocks contained in the fault zone.

### *Deformation of quartz-rich lenses*

Data collected using EBDS and from microcomposition allowed the distinction between two generations of quartz formation. The strong internal misorientation of the large host quartz grains reveals their pre-kinematic origin. The mechanism of deformation was predominantly semi-brittle produced by slip plane. Small quartz grains grew inside the microfractures of the large quartz grains formed by the cataclasis related to the fault activity. The fast growth of their *c* axis looking for the available space inside the fractures produced slight orientation. From a compositional point of view small quartz grains included in veins are enriched in Al, As and Sb, which is in agreement with the suggested changes produced by hydrothermal alteration. Significant amounts of these elements have also been found in quartz associated with hydrothermal processes (Lubben *et al.*, 2012). Feldspar dissolution or replacement by clay minerals has been suggested as a source of the Al in quartz (Goette *et al*., 2013). The incorporation of Al in authigenic quartz is controlled by the activity of Al in the aqueous solution which is, assuming equilibrium

https://doi.org/10.1180/claymin.2015.050.5.06 Published online by Cambridge University Press

conditions, determined by the stable Al-mineral, the pH buffered by carbonates and dissolved $CO_2$, and *PT* conditions (Rusk *et al*., 2008). The absence of authigenic clay minerals paragenetic with quartz in veins enables the role of quartz as a sink for the Al.

### *Carbonate and sulfate cementation*

Textural and EBSD data suggest a final stage of post-kinematic dolomite crystallization in the highly damaged areas of the microcataclasites which sealed the microfractures. This stage could be related to low-temperature and high-salinity water circulation episodes, suggesting that cataclasis may control pathways and focus water circulation in the fault system. These waters might be related to carbonate dissolution along deep faults (*e.g.* Cerón *et al*. 2000, Hernández-Puentes *et al.*, 2015) as indicated by the abnormal boron concentration. The occurrence of thermal waters along this fault area appears to be favoured by the great depth of the fractures affecting the substratum. This allows the rise of groundwater enriched in $CO_2$ gas. Saturation and oversaturation in carbonate materials (calcite and dolomite) of the waters circulating through the fault zone (Table 6) facilitate the dolomite sealing of the microfractures generated by fault deformation. The existence of carbonate and/or quartz-rich veins with crack-and-seal texture has been observed widely in the past, indicating the presence of fluid-assisted fracturing and cementation processes in fault materials (*e.g.* Vannucchi *et al*., 2008; Fagereng *et al*., 2010). These mineralizing events cemented formerly active sliding surfaces and could affect the global frictional strength of the fault rock. However, Tesei *et al*. (2012) suggested that slip is favoured energetically to proceed along weak phyllosilicate layers present in the rock without re-shearing the cemented materials. Therefore, the presence of localized phyllosilicates in rocks with mostly quartzo-feldspathic mineral composition, favours sealing processes which would have a limited effect, given that there are thousands of weak potential sliding surfaces associated with their 001 planes.

### *Concluding remarks*

Petrographic (enrichment in chlorite that is crystallized as patches) and geochemical (Mg, Fe, water, As and Zn enrichment) characteristics of the quartz-rich rocks from the Carboneras and Palomares fault-zones suggest that the damaged rocks underwent chloritization associated with the hydrothermal activity promoted by the volcanic activity of the Cabo de Gata belt.

Hydrothermal alteration occurred before the rocks studied were affected by the main fault movements. The absence of syn-kinematic crystallization of phyllosilicates reveals that their influence was restricted to providing weakened areas with lubricating properties, which favoured creep movements that reduced the possibility of large seismic events. Sealing produced by mineralizing events, such as dolomite cementation as a consequence of the fluid–rock interaction processes, would have had a limited effect due to the presence of localized weak bands of phyllosilicates favouring the formation of sliding surfaces.

## ACKNOWLEDGEMENTS

The authors are grateful to M.M. Abad and I. Guerra (C.I.C., Univ. Granada) for their help with HRTEM and SEM work. C. Laurin is thanked for editing the English. The authors also acknowledge Elisabetta Mariani for providing access to the University of Liverpool facilities and for helping with EBSD data. A constructive review by F. Nieto is gratefully acknowledged. Financial support was provided by Research Project CGL2011-30153-C02-01 (Spanish Ministry of Economy and Competitiveness) and the Junta de Andalucía Research Group RNM-325.

## REFERENCES

Bedrosian P.A., Unsworth M.J., Egbert G.D. & Thuerber C.H. (2004) Geophysical images of creeping segment of the San Andreas Fault: Implications for the role of crustal fluids in the earthquake process. *Tectonophysics*, **385**, 137–158.

Benito R., Garcia-Guinea J., Valle-Fuentes F.J. & Recio P. (1998) Mineralogy, geochemistry and uses of the mordenite-bentonite ash-tuff beds of Los Escullos, Almeria, Spain. *Journal of Geochemical Exploration*, **62**, 229–240.

Bolognesi L. (1997) A tentative correlation between seismic activity and changes in the composition of thermal waters on Vulcano Island, Italy. *Geothermics*, **26**, 379–392.

Bourdelle F., Parra T., Chopin C. & Beyssac O. (2013) A new chlorite geothermometer for diagenetic to low-grade metamorphic conditions. *Contributions to Mineralogy and Petrology*, **165**, 723–735.

Brace W.F., Paulding Jr. B.W. & Scholz C. (1966) Dilatancy in the fracture of crystalline rocks. *Journal of Geophysical Research*, **71**, 3939–3953.

Brumm M., Wang C.Y. & Manga M. (2009) Spring temperatures in the Sagehen Basin, Sierra Nevada, CA: Implications for heat flow and groundwater circulation. *Geofluids*, **9**, 195–207.

https://doi.org/10.1180/claymin.2015.050.5.06 Published online by Cambridge University Press

Byerlee J. (1978) Friction of rocks. *Pure and Applied Geophysics*, **116**, 615–626.

Cerón J.C., Martín-Vallejo M. & García-Rossell L. (2000) $CO_2$-rich thermomineral groundwater in the Betic Cordilleras, southeastern Spain: Genesis and tectonic implications. *Hydrogeology Journal*, **8**, 209–217.

Chester F., Evans J.P. & Biegel R.L. (1993) Internal structure and weakening mechanisms of the San Andreas Fault. *Journal of Geophysical Research*, **98**, 771–786.

Cliff G. & Lorimer G.W. (1975) The quantitative analyses of thin specimens. *Journal of Microscopy*, **103**, 203–207.

Clark I. & Fritz P. (2000) *Environmental Isotopes in Hydrogeology.* Lewis, New York. 328 pp.

Correns C.W. (1978) Titanium: behavior in metamorphic reactions. pp. 22-H in: *Handbook of Geochemistry*, **1** (K.H. Wedepohl, editor). Springer, Berlin.

Dieterich J.H. & Kilgore B.D. (1994) Direct observation of frictional contacts: New Insights for state-dependent properties. *Pure and Applied Geophysics*, **143**, 283–302.

Dostal J., Strong D.F. & Jamieson R.A. (1980) Trace element mobility in the mylonite zone within the ophiolite aureole, St. Anthony complex, Newfoundland. *Earth and Planetary Science Letters*, **49**, 188–192.

Duggen S., Hoernle K. & Van der Bogaard, H. (2004) Magmatic evolution of the Alboran region: The role of subduction in forming the western Mediterranean and causing the Messinian Salinity Crisis. *Earth and Planetary Science Letters*, **218**, 91–108.

Fagereng A., Remitti F. & Sibson R.H. (2010) Shear veins observed within anisotropic fabric at high angles to the maximum compressive stress. *Nature Geoscience*, **3**, 482–485.

Faulkner D.R. & Rutter E.H. (2001) Can the maintenance of overpressured fluids in large strike-slip fault zones explain their apparent weakness? *Geology*, **29**, 503–506.

Faulkner D.R., Mitchell T.M., Hirose T. & Shimamoto T. (2009) The frictional properties of phyllosilicates at earthquake slip speeds. *Geophysical Research Abstracts*, **11**, EGU2009-5751-3.

Floyd P.A. & Winchester, J.A. (1983) Element mobility associated with meta-shear zones within the Ben Hope amphibolite suite. *Scotland. Chemical Geology*, **39**, 1–15.

Glazner A.F. & Bartley, J.M. (1991) Volume loss, fluid flow and state of strain in extensional mylonites from the central Mojave Desert, California. *Journal of Structural Geology*, **13**, 587–594.

Goette T., Ramseyer K. & Pettke T. (2013) Implications of trace element composition of syntaxial quartz cements for the geochemical conditions during quartz precipitation in sandstones. *Sedimentology*, **60**, 1111–1127.

Gracia E., Palla R., Soto J.I., Comas M., Moreno X., Masana E., Santanach P., Diez S., García M., Dañobeitia J. & HITS scientific party (2006) Active faulting offshore SE Spain (Alboran Sea): Implications for earthquake hazard assessment in the Southern Iberian Margin. *Earth and Planetary Science Letters*, **241**, 734–749.

Grant J.A. (1986) The isocon diagram. A simple solution to Gresen's equations for metasomatic alteration. *Economic Geology*, **81**, 1976–1982.

Gresens R.L. (1967) Composition-volume relations of metasomatism. *Chemical Geology*, **2**, 47–65.

Hernández-Puentes P., Jiménez-Espinosa R. & Jiménez-Millán J. (2015) Geochemical patterns of groundwater from the Palomares–Carboneras active fault area aquifers (SE Spain): determination of a network of sensitive sites indicators of seismic events. *Environmental Earth Sciences*, **73**, 6341–6354.

Humphris S.E., Alt J.C., Teagle D.A.H. & Honnorez J.J. (1998) Geochemical changes during hydrothermal alteration of basement in the stockwork beneath the active TAG hydrothermal mound (P.M. Herzig, S.E. Humphris, D.J. Miller & R.A. Zierenberg, editors). Pp. 255–276 in: Proceedings of the Ocean Drilling Programme Scientific Results, **158**.

Ikari M., Niemeijer A. & Marone C. (2011) The role of fault zone fabric and lithification state on frictional strength, constitutive behavior, and deformation microstructure. *Journal of Geophysical Research*, **116**, B08404.

Inoue A., Meunier A., Patrier-Mas P., Rigault C., Beaufort D. & Vieillard P. (2009) Application of chemical geothermometry to low temperature trioctahedral chlorites. *Clays and Clay Minerals*, **57**, 371–382.

IGN (2001) Instituto Geográfico Nacional, *Catálogo Sísmico Nacional hasta el 1900*. Madrid, Spain, http://www.ign.es/ign/resources/sismologia/publicaciones/Catalogohasta1900.pdf

Italiano F., Bonfanti P., Pizzino L. & Quattrocchi F. (2010) Geochemistry of fluids discharged over the seismic area of the Southern Apennines (Calabria region, southern Italy): Implications for fluid-fault relationships. *Applied Geochemistry*, **25**, 540–554.

Karner S.L., Marone C. & Evans B. (1997) Laboratory study of fault healing and lithification in simulated fault gouge under hydrothermal conditions. *Tectonophysics*, **277**, 41–55.

Kretz R. (1983) Symbols for rock-forming minerals. *American Mineralogist*, **68**, 277–279.

Lachenbruch A.H. & Sass J.H. (1988) The stress heat-flow paradox and thermal results from Cajon Pass. *Geophysics Research Letter*, **15**, 981–984.

Lackschewitz K.S., Singer A., Botz R., Garbe-Schönberg D. & Stoffers P. (2000) Mineralogical and geochemical characteristics of clay minerals in the region of a major hydrothermal site in the Escanaba Trough, Gorda Ridge, northeast Pacific Ocean, Leg 169. Pp. 1–24 in: Proceedings of the ODP Scientific Results, 169 (R.A. Zierenberg, Y. Fouquet, D.J. Miller & W.R. Normark, editors).

https://doi.org/10.1180/claymin.2015.050.5.06 Published online by Cambridge University Press

Lackschewitz K.S., Devey C.W., Stoffers P., Botz R., Eisenhauer A., Kummetz M., Schmidt M. & Singer A. (2004) Mineralogical, geochemical and isotopic characteristics of hydrothermal alteration processes in the active, submarine, felsic-hosted PACMANUS field, Manus Basin, Papua New Guinea. *Geochimica et Cosmochimica Acta*, **68**, 4405–4427.

Lanari P., Wagner T. & Vidal O. (2014) A thermodynamic model for di-trioctahedral chlorite from experimental and natural data in the system MgO–FeO–$Al_2O_3$–$SiO_2$–$H_2O$: applications to P–T sections and geothermometry. *Contributions to Mineralogy and Petrology*, **167**, 968.

Lloyd G., Geoffrey E. & Knipe R.J. (1992) Deformation mechanisms accommodating faulting of quartzite under upper crustal conditions. *Journal of Structural Geology*, **14**, 127–143.

Lubben J.D., Cline J.S. & Barker S.L. (2012) Ore fluid properties and sources from quartz-associated gold at the Betze-Post Carlin-Type Gold Deposit, Nevada, United States. *Economic Geology*, **107**, 1351–1385.

Manga M. & Rowland J.C. (2009) Response of Alum Rock Springs to the October 30, 2007 Alum Rock earthquake and implications for the origin of increased discharge after earthquakes. *Geofluids*, **9**, 237–250.

Masana E., Martínez-Díaz J.J., Hernández-Enrile J.L. & Santanach P. (2004) The Alhama de Murcia fault (SE Spain), a seismogenic fault in a diffuse plate boundary: Seismotectonic implications for the Ibero–Magrebian region. *Journal of Geophysical Research*, **109**, 1–17.

Montenat C. & Ott D'Estevou P. (1995) Late Neogene basins evolving in the Eastern Betic transcurrent fault zone: An illustrated review. Pp. 372–386 in: *Tertiary Basins of Spain* (P.F. Friend & C.J. Dabrio, editors). Cambridge University Press, Cambridge, UK.

Montgomery D.R. & Manga M. (2003) Streamflow and water well responses to earthquakes. *Science*, **300**, 2047–2049.

Mook W.G., Gat J.R., Roznski K., Froehlich K., Geyh M., Séller K.L. & Konikow L.F. (2002) *Isótopos Ambientales en el Ciclo Hidrológico. Principios y Aplicaciones.* W.G. Publicaciones IGME, Madrid, Spain 596 pp.

Morales-Ruano S.M., Rosua F.J.C. & Hach-Ali P.F. (2000) Epithermal Cu-Au mineralization in the Palai-Islica deposit, Almeria, southeastern Spain: Fluid-inclusion evidence for mixing of fluids as a guide to gold mineralization. *The Canadian Mineralogist*, **38**, 553–565.

Morrow C.A., Moore D.E. & Lockner D.A. (2000) The effect of mineral bond strength and adsorbed water on fault gouge frictional strength. *Geophysical Research Letters*, **27**, 815–818.

Morrow C.A., Shi L.Q. & Byerlee J.D. (1984) Permeability of fault gouge under confining pressure and shear stress. *Journal of Geophysical Research*, **89**, 3193–3200.

Muhuri S.K., Dewers T.A., Scott T.E. & Reches Z. (2003) Interseismic fault strengthening and earthquake-slip instability: Friction or cohesion? *Geology*, **31**, 881–884.

Nieto F., Ortega-Huertas M., Peacor D.R. & Aróstegui J. (1996) Evolution of illite/smectite from early diagenesis through incipient metamorphism in sediments of the Basque-Cantabrian Basin. *Clays Clay Minerals*, **44**, 304–323.

O'Hara K. (1988) Fluid flow and volume loss during mylonitization: an origin for phyllonite in an overthrust setting, North Carolina, U.S.A. *Tectonophysics*, **156**, 21–36.

O'Hara K. & Blackburn W.H. (1989) Volume loss model for trace element enrichment in mylonites. *Geology*, **17**, 524–527.

Olsen M., Scholz C.H. & Lèger A. (1998) Healing and sealing of a simulated fault gouge under hydrothermal conditions: Implications for fault healing. *Journal of Geophysical Research*, **103**(B4), 7421–7430.

Rusk B.G., Lowers H.A. & Reed M.H. (2008) Trace elements in hydrothermal quartz: relationships to cathodoluminescent textures and insights into vein formation. *Geology*, **36**, 547–550.

Rutter E.H., Maddock R.H., Hall S.H. & White S.H. (1986) Comparative microstructures of natural and experimentally produced clay-bearing fault gouges. *Pure and Applied Geophysics*, **124**, 3–30.

Rutter E.H., Burgess R. & Faulkner D.R. (2014) Constraints on the movement history of the Carboneras Fault Zone (SE Spain) from stratigraphy and $^{40}Ar$–$^{39}Ar$ dating of Neogene volcanic rocks. Pp. 79–99 in: *Deformation Structures and Processes within the Continental Crust* (S. Llana –Fúnez, A. Marcos & F. Bastida, editors). Special Publication, **394**, Geological Society, London.

Sánchez-España J., Velasco F. & Yusta I. (2000) Hydrothermal alteration of felsic volcanic rocks associated with massive sulphide deposition in the northern Iberian Pyrite Belt (SW Spain). *Applied Geochemistry*, **15**, 1265–1290.

Sanz de Galdeano C. (1990) Geologic evolution of the Betic Cordilleras in the western Mediterranean, Miocene to present. *Tectonophysics*, **172**, 107–119.

Schleicher A.M., Van der Pluijm B.A., Solum J.G. & Warr L.N. (2006) The origin and significance of clay minerals on surfaces, in fractures and in veins from SAFOD borehole samples (Parkfield, California). *Geophysical Research Letters*, **33**, L16313.

Sibson R.H. (1990) Conditions for fault-valve behaviour. Pp. 15–28 in: *Deformation Mechanisms, Rheology and Tectonics* (R.J. Knipe & E.H. Rutter, editors). Special Publications, 54, Geological Society, London.

Singh C.K., Rina K., Singh R.P. & Mukherjee S. (2014) Geochemical characterization and heavy metal

https://doi.org/10.1180/claymin.2015.050.5.06 Published online by Cambridge University Press

contamination of groundwater in Satluj River Basin. *Environmental Earth Sciences*, **71**, 201–216.

Sinha A.K., Hewitt D.A. & Rimstidt J.D. (1986) Fluid interaction and element mobility in the development of ultramylonites. *Geology*, **14**, 833–886.

Solum J.G. & Van der Pluijm B.A. (2004) Phyllosilicate mineral assemblages of the SAFOD Pilot Hole and comparison with an exhumed segment of the San Andreas Fault System. *Geophysical Research Letters*, **31**, L15S19.

Tesei T., Collettini C., Carpenter B.M., Viti C. & Marone C. (2012) Frictional strength and healing behavior of phyllosilicate-rich faults. *Journal of Geophysical Research*, **117**, B09402.

Uehara S.I. & Shimamoto, T. (2004) Gas permeability evolution of cataclasite and fault gouge in triaxial compression and implications for changes in fault-zone permeability structure through the earthquake cycle. *Tectonophysics*, **378**, 183–195.

Vannucchi P., Remitti F. & Bettelli G. (2008) Geological record of fluid flow and seismogenesis along an erosive subducting plate boundary. *Nature*, **451**, 699–703.

Vidal O., Parra T. & Vieillard P. (2005) Thermodynamic properties of the Tschermak solid solution in Fe-chlorite: application to natural examples and possible role of oxidation. *American Mineralogist*, **90**, 347–358.

Vidal O., de Andrade V., Lewin E., Muñoz M., Parra T. & Pascarelli S. (2006) P-T-deformation-Fe3+/Fe2+ mapping at the thin section scale and comparison with XANES mapping: application to a garnet-bearing metapelite from the Sambagawa metamorphic belt (Japan). *Journal of Metamorphic Geology*, **24**, 669–683.

Walker R.J., Holdsworth R.E., Imber J., Faulkner D.R. & Armitage P.J. (2013) Fault zone architecture and fluid flow in interlayered basaltic volcaniclastic crystalline sequences. *Journal of Structural Geology*, **51**, 92–104.

Wang C.Y. (1984) On the constitution of the San Andreas fault zone in central California. *Journal of Geophysical Research*, **89**, 5858–5866.

Warr L.N. & Cox S. (2001) Clay mineral transformations and weakening mechanisms along the Alpine Fault, New Zealand. Pp. 85–101 in: *The Nature and Tectonic Significance of Fault Zone Weakening* (R.E. Holdsworth, R.A. Strachan, J.F. Magloughlin & R.J. Knipe, editors). Special Publications, 186, Geological Society, London.

Winchester J.A. & Max M.D. (1984) Element mobility associated with syn-metamorphic shear zones near Scotchport, NW Mayo, Ireland. *Journal of Metamorphic Geology*, **2**, l–11.

Wu F.T., Blatter L. & Robertson H. (1975) Clay gouges in the San Andreas Fault system and their possible implications. *Pure and Applied Geophysics*, **113**, 87–96.

Yuce G. (2007) A geochemical study of the groundwater in the Misli basin and environmental implications. *Environmental Geology*, **51**, 857–868.

Zhang S. & Cox S.F. (2000) Enhancement of fluid permeability during shear deformation of a synthetic mud. *Journal of Structural Geology*, **22**, 1385–1393.

Zhang S., Tullis T.E. & Scruggs V.J. (1999) Permeability anisotropy and pressure dependency of permeability in experimentally sheared gouge materials. *Journal of Structural Geology*, **21**, 795–806.

Zoback M.D. (2000) Strength of the San Andreas. *Nature*, **405**, 31–32.

https://doi.org/10.1180/claymin.2015.050.5.06 Published online by Cambridge University Press